A search for thermal gyro-synchrotron emission from hot stellar coronae

Walter Golay[1]★, Robert L. Mutel[1], Dani Lipman[1,2], and Manuel Güdel[3]
[1]Department of Physics and Astronomy, University of Iowa, Iowa City IA 52242, USA
[2]Department of Physics, University of Connecticut, 196A Auditorium Road, Unit 3046, Storrs, CT 06269, USA
[3]Department of Astrophysics, University of Vienna, Türkenschanzstrasse 17 A-1180 Vienna, Austria

Accepted XXX. Received YYY; in original form ZZZ

ABSTRACT

We have searched for thermal gyro-synchrotron radio emission from a sample of five radio-loud stars whose X-ray coronae contain a hot ($T > 10^7$ K) thermal component. We used the JVLA to measure Stokes I and V/I spectral energy distributions (SEDs) over the frequency range 15–45 GHz, determining the best-fitting model parameters using power-law and thermal gyro-synchrotron emission models. The SEDs of the three chromospherically active binaries (Algol, UX Arietis, HR 1099) were well-fit by a power-law gyro-synchrotron model, with no evidence for a thermal component. However, the SEDs of the two pre-main-sequence (PMS) stars (V410 Tau, HD 283572) had a circularly polarized enhancement above 30 GHz that was inconsistent with a pure power-law distribution. These spectra were well-fit by summing the emission from an extended coronal volume of power-law gyro-synchrotron emission and a smaller region with thermal plasma and a much stronger magnetic field emitting thermal gyro-synchrotron radiation. We used Bayesian inference to estimate the physical plasma parameters of the emission regions (characteristic size, electron density, temperature, power-law index, and magnetic field strength and direction) using the independently VLBI-measured radio sizes, X-ray luminosity, and magnetic field strength as priors, where available. The derived parameters were well-constrained but highly degenerate. The best-fitting temperatures for both PMS stars were ~ 0.5 dex higher than the X-ray-derived temperatures. We argue that the power-law and thermal volumes in the PMS stars are probably not co-spatial and speculate that they may arise from two distinct regions, the stellar corona and the inner edge of their accretion disc, respectively.

Key words: radiation mechanisms:general – stars:coronae – radio continuum:stars – magnetic fields – plasmas – techniques:spectroscopic

1 INTRODUCTION

Non-thermal radio emission from stars is a powerful diagnostic for investigating high-energy processes in stellar coronae. In particular, gyro-synchrotron and synchrotron radiation from high-energy electrons spiraling in strong coronal magnetic fields is a common feature of many stellar systems ranging from 'normal' stars like the Sun (Bastian et al. 1998) to evolved pre-main-sequence stars (Launhardt et al. 2022), close late-type binaries (Drake et al. 1992), and even ultra-cool dwarfs near the bottom of the main-sequence (Williams 2018).

The energetic electrons typically follow a power-law energy distribution, presumably accelerated by reconnection of magnetic fields in the corona. The accelerated electrons have energies with Lorentz factors of order 10-100, i.e., mildly relativistic, so the radiation is referred to as gyro-synchrotron (GS) emission. This mechanism has been well-studied in a range of stellar environments. The observed spectral energy distributions (SEDs) and polarization have allowed quantitative estimates of the magnetic field strength and energetic particle densities in the solar and stellar coronae (e.g., Umana et al. 1993; Storey & Hewitt 1995; Mutel et al. 1998; Trigilio et al. 2001; García-Sánchez et al. 2003; Osten & Bastian 2006; Leto et al. 2006; Waterfall et al. 2019; Launhardt et al. 2022; Tan 2022).

A less well-known emission mechanism is gyro radiation from *thermal* electrons spiraling in a stellar magnetic field. If the electrons are non-relativistic, the radiation is called gyro-resonance, and emission (and absorption) occurs at the local electron gyro frequency, and its first few harmonics. Solar flares have demonstrated gyro-resonance emission (e.g., Nindos et al. 2000), often at the third harmonic.

For very hot plasmas ($T \gtrsim 10^7$ K), there are a significant number of electrons in the high-energy tail of a Maxwellian energy distribution, and since they are mildly relativistic, they radiate at low harmonics of the gyro-frequency. The resulting radiation–which can be highly circularly polarized depending on the aspect angle–is termed thermal gyro-synchrotron radiation (Dulk 1985). Since thermal GS emission strongly depends on the magnetic field strength and coronal temperature, its detection can provide a sensitive measure of these quantities independent of assumptions about a power-law electron distribution.

For stars with X-ray-derived coronal temperatures, a thermal GS detection can characterize the coronal magnetic field or provide an upper limit for non-detection. Likewise, thermal GS measurements can estimate coronal temperature for stars with measured coronal magnetic field strengths and extent derived from, for ex-

★ Email: walter-golay@uiowa.edu

ample, Zeeman-Doppler imaging (Donati & Semel 1990). A few previous papers have reported the detection of thermal GS emission, but mainly in solar flares (Dulk et al. 1979; Kobayashi et al. 2006; Tan 2022). Drake et al. (1992) considered whether thermal GS can explain the spectral properties of low-level radio emission from RS CVn binary stars but reached no conclusion.

In this paper, we report on a search for thermal GS emission from five radio-loud stars that we selected based on previously-published detection of high coronal temperature and strong magnetic fields. The stars comprised two classes: chromospherically active binaries (Algol, UX Arietis, HR 1099) and weak-line T-Tauri pre-main-sequence stars (V410 Tau, HD 283572). The observations sample the spectral energy distributions in Stokes I and V over a wide range of frequencies. We fit the observed SEDs with model SEDs generated by a two-component emission model consisting of a mildly relativistic population with a power-law electron energy distribution and a hot thermal component with a Maxwellian energy distribution. Each model had five free parameters that parametrized the best fit to the observed SEDs. For convenience, we include the `Python` code used to generate each figure, found on this Github repository and archived on Zenodo doi:10.5281/zenodo.7222487.

2 GYRO-SYNCHROTRON RADIATION: SUMMARY OF PROPERTIES

The derivation of the volume emission (η_ν) and linear absorption (κ_ν) coefficients for GS radiation, whether by power-law or thermal electron distributions, is notoriously difficult, since it involves integrals over infinite sums of Bessel functions. However, several clever approximation methods have been developed that have made this calculation tractable (e.g., Trubnikov 1958; Dulk et al. 1979; Petrosian 1981; Leung et al. 2011).

Robinson & Melrose (1984) derived analytic expressions for GS coefficients for both power-law and thermal electron distributions based on these approximations. We have used these expressions to calculate the expected SED and polarization for a homogeneous magneto-active plasma volume with electron energy populations consisting of (1) a hot isothermal plasma or (2) a plasma with a power-law energetic electron population viz.,

$$n_p(E)dE = n_p \cdot \frac{\delta - 1}{E_0}\left[\frac{E}{E_0}\right]^{-\delta} dE \tag{1}$$

where n_p is power-law electron density and E_0 is the minimum cutoff energy, we assume $E_0 = 10$ keV. For each volume, we solve the equation of radiative transfer along the lines of sight intercepting the coronal plasma using the Robinson & Melrose (1984) expressions for η_ν and κ_ν.

Note that we do not discuss the contribution of bremsstrahlung (free-free) radiation since in all cases considered in this work, bremsstrahlung contributes less than 1% of the total flux density.

2.1 Maxwellian electron distributions

The (SED) for radiation emitted by a non-relativistic thermal plasma in a magnetic field ('gyro-resonance radiation') is the sum of contributions from individual electrons emitting at the local gyro frequency and the first few harmonics. The radiation is largely circularly polarized at aspect angles outside the plane of rotation. However, as the plasma temperature exceeds $T \sim 10^7$ K, a significant fraction of the electron population becomes relativistic. This case significantly modifies both the SED and polarization. At large optical depth, the SED is a power-law with spectral index $\alpha = +2$ and is steeply negative ($\alpha \sim -15$) at a small optical depth. The peak flux occurs near $\tau = 2.5$, where τ is approximately given by,

$$\tau_\nu \sim 1.2\left[\frac{T}{10^8 K}\right]^7 \cdot \left[\frac{B}{kG}\right]^9 \cdot \left[\frac{\nu}{10\ \mathrm{GHz}}\right]^{-10} \cdot \left[\frac{n_e}{10^5\ \mathrm{cm}^{-3}}\right] \cdot \left[\frac{L}{R_\odot}\right] \tag{2}$$

where T is the plasma kinetic temperature, B is the magnetic field strength, ν is the frequency, n_e is the thermal electron density, and L is the depth along the line of sight to the observer.

The frequency at SED maximum can be written approximately as

$$\nu_{\mathrm{peak}} \sim 10\ \mathrm{GHz} \cdot \left[\frac{\mathrm{B}}{\mathrm{kG}}\right] \cdot \left[\frac{\mathrm{T}}{10^7 \mathrm{K}}\right]^{0.5} \cdot \sin^{0.6}(\theta) \tag{3}$$

where we have combined equations 32a,b of Dulk (1985). Note that the peak frequency depends only on the magnetic field and plasma temperature and is insensitive to density or path length.

The polarization is elliptical, but the axial ratios for ordinary and extraordinary modes are close to unity unless the propagation direction is nearly perpendicular to the magnetic field. This effect results in circularly polarized modes for propagation angles θ that satisfy (Robinson & Melrose 1984),

$$|\theta - \pi/2| \gg \frac{\nu_B}{2\nu} \tag{4}$$

where ν is the emission frequency, and ν_B is the electron gyrofrequency. The polarization fraction is relatively high, typically 40–90 per cent for a homogeneous plasma near the peak emission frequency, but decreases sharply with increasing optical depth and is nearly zero for $\tau \gg 1$.

Inspection of Equation 2 and Equation 3 indicate that we expect thermal GS radiation to be most prominent for very hot (>10 MK) coronal plasmas with strong (~ kG) magnetic fields. The SEDs will have spectral peaks above 10 GHz and be circularly polarized. Sample model thermal GS spectra (Stokes I and V/I) are shown in Figure 1 for uniform magnetic fields of 0.5 kG and 1.5 kG, and for plasma temperatures 33 MK and 100 MK.

2.2 Power-law electron distributions

The spectral energy distribution of radiation by highly relativistic power-law electrons in a magneto-plasma is well-known, consisting of a rising spectrum with $\alpha = +5/2$ at large optical depth, a falling spectrum with $\alpha = (1 - \delta)/2$ at small optical depth, and a peak near $\gamma^2 \nu_B$ where γ is the Lorentz factor and ν_B is the gyro frequency. Relativistic beaming confines the radiation to small angles perpendicular to the magnetic field, resulting in linear polarization.

The SED and polarization characteristics are significantly different for mildly relativistic power-law electron distributions (frequencies roughly 10x-100x the electron gyrofrequency). At large optical depths, the SED is also a power-law but with a somewhat steeper slope ($\alpha = 2.5 + 0.085\delta$, Dulk 1985). At small optical depth, the slope α is also somewhat steeper than the fully relativistic case,

$$\alpha \sim 1.6 - \frac{(1 - \delta)^{1.25}}{2} \tag{5}$$

Power-law GS radiation is circularly polarized for propagation angles that satisfy Equation 4. For a uniform magnetic field and $\tau \ll 1$, the fractional polarization varies from $V/I \sim 0.9$ at low harmonics and steep power-law index to $V/I < 0.1$ for high harmonics and shallow index. These fractions pertain to plasmas with unidirectional magnetic fields. Of course more realistic magnetic geometries will result in lower fractions.

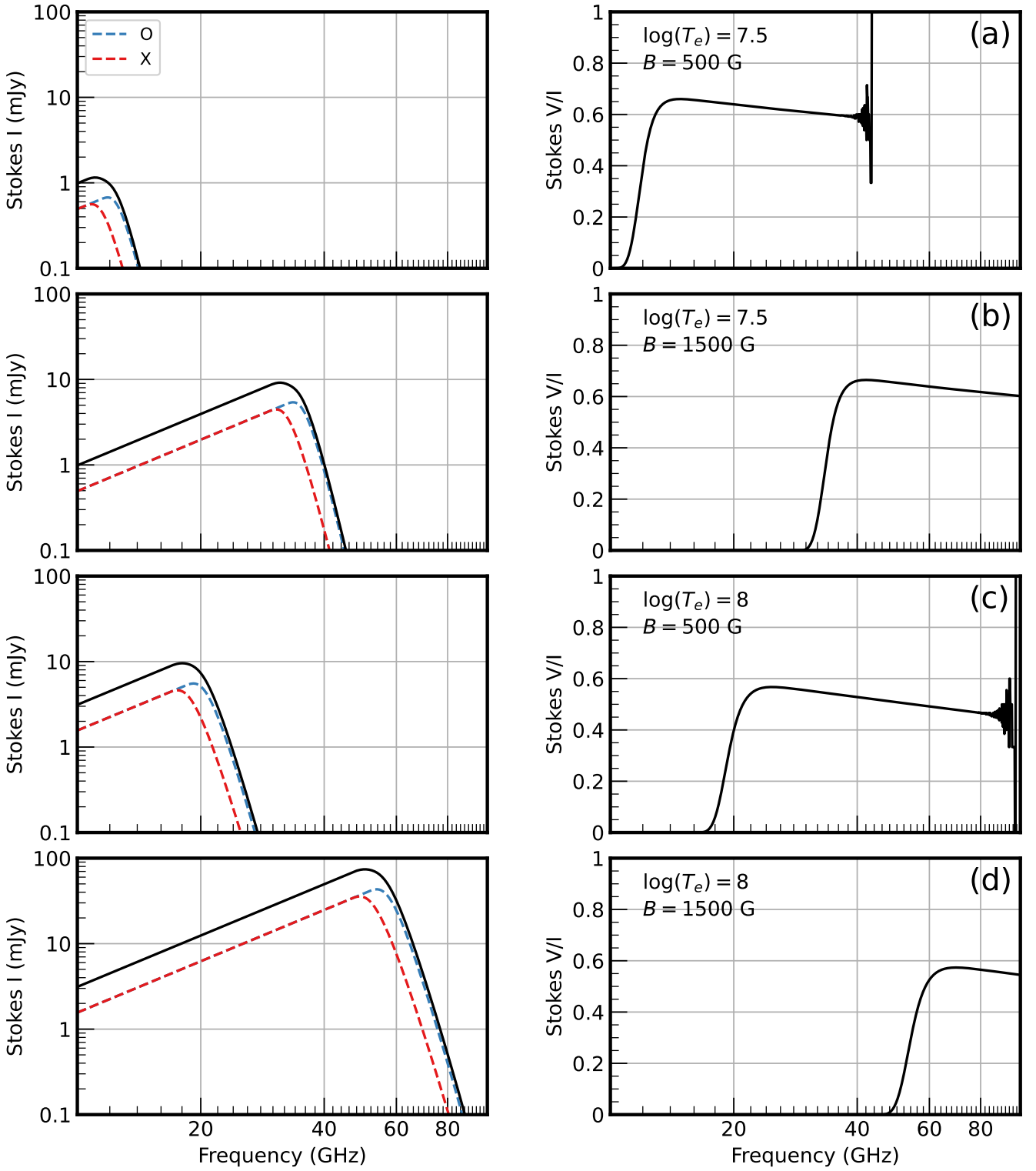

Figure 1. Stokes I spectral energy density distributions (left panels) and fractional circular polarization (right panels) for thermal GS emission from a homogeneous stellar corona modeled as a uniform cube with sides $1\,R_\odot$ at a distance 10 pc, with constant electron density $n_e = 10^{10}\,\mathrm{cm}^{-3}$, and uniform magnetic field oriented 80° inclination to the observer's line of sight. (a) B = 500 G, $T_e = 10^{7.5}$ K, (b) B= 500 G, $T_e = 10^8$ K, (c) B = 1500 G, $T_e = 10^{7.5}$ K, (d) B = 1500 G, $T_e = 10^8$ K. The Stokes I plot lines are X-mode (dashed red line), O-mode (dashed blue line), and total thermal GS emission (solid black line). Numerical instability in the fractional polarization at high frequency is due to the total flux approaching zero.

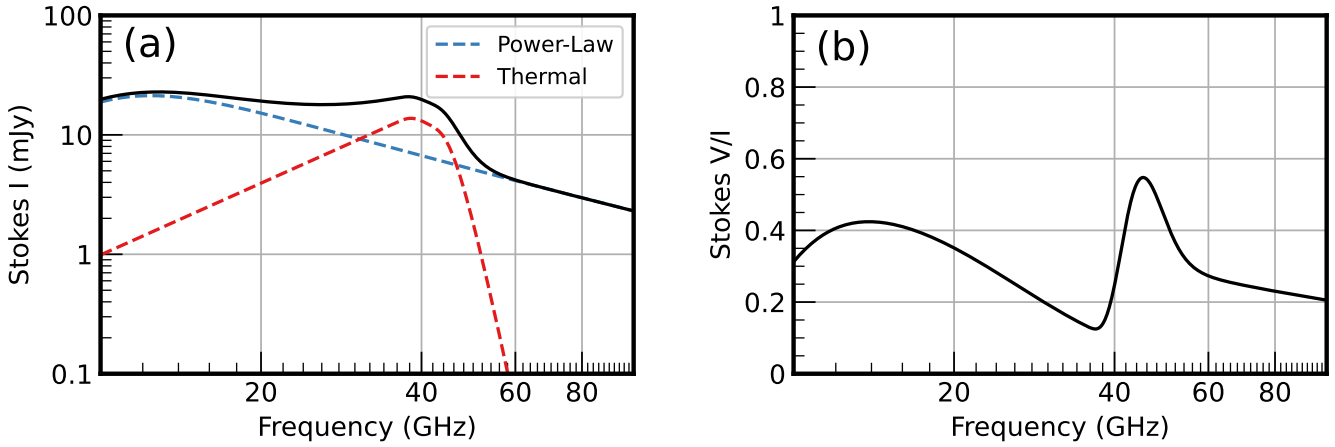

Figure 2. (a) Stokes I spectral energy distributions for the sum of two uniform plasma volumes with different emission processes: power-law GS emission (dotted blue line) and thermal GS emission (dotted red line). Both plasma models are uniform cubes with sides 1 $R_\odot$ at 10 pc distance. The power-law region has density $n_e = 10^7$ cm^{-3}, energy index $\delta = 3$, and a 200 G magnetic field. The thermal box has an electron density $n_e = 10^{10}$ cm^{-3}, a temperature $T_e = 10^{7.5}$ K, and a 2 kG magnetic field strength. The magnetic field is oriented at 45° and 60° to the observer's line of sight, respectively. (b) The corresponding fractional circular polarization (Stokes V/I) of the combined emission demonstrates the relatively narrow but substantial peak characteristic of thermal GS emission near the emission peak frequency.

2.3 Spectral energy distribution and polarization for combined thermal and power-law GS emission

In this paper, we will consider whether observed SEDs from stellar coronae result from GS emission from power-law electrons (as is often invoked), or whether the spectra are a composite of emission from different regions dominated by power-law and hot thermal electrons. Figure 2 shows a representative composite spectrum consisting of the sum of SEDs from two equal spatially distinct volumes, a cube with dimension one solar radius on each side:

- A power-law GS emission region with parameters: $n_e = 10^7$ cm^{-3}, $\delta = 3$, B = 200 G; dashed blue line) with a turnover near unity optical depth, and
- A thermal GS emission from a denser region of hot thermal plasma and high magnetic field strength ($n_e = 10^{10}$ cm^{-3}, T = $10^{7.5}$ K, B = 2 kG; dashed red line).

For this example, the thermal GS peak is somewhat near the power-law SED peak and has a similar peak flux density, so it may be challenging to distinguish between these emissions. However, a key difference is the degree of circular polarization, which sharply peaks near the thermal GS spectral peak. The key distinguishing feature of thermal GS emission is this sharp rise in fractional circular polarization near the spectral peak.

3 OBSERVATIONS AND DATA REDUCTION

We observed five stars with previous radio detections. We selected the target list based on two criteria: (1) The star had sufficient X-ray spectral information to be consistent with a hot component $T \sim 10^7$ K or higher, (2) The star had evidence for kilogauss magnetic fields, inferred from Zeeman-Doppler imaging (ZDI) or non-thermal radio emission.

We observed each star with the JVLA using six frequency bands spanning a total of two hours with the following cadence: Ku band (14–16 GHz), 3 min; K band (22–24 GHz), 6 min; Ka lower band (29–30 GHz and 32–33 GHz), 6 min; Ka upper band (34–36 GHz), 9 min; Q lower band (40–42 GHz), 15 min; and Q upper band (44–46 GHz), 18 min. We chose the varying integration times to account for the decreasing sensitivity of the JVLA at higher frequencies. The observations spanned a total of five 2-hour intervals (Table 1). We used the CASA software suite (McMullin et al. 2007) to edit, calibrate, and image each field. We determined Stokes I and V fluxes using 2-dimensional Gaussian fits and corresponding uncertainties. Table 2 summarizes the resulting flux densities and uncertainties.

4 ANALYSIS: MODEL FITTING

To determine the physical properties of the plasma responsible for the observed emission, we fit the observed SEDs and polarizations by calculating the emergent flux and polarization for a uniform plasma with prescribed physical parameters, adjusting each parameter to fit the observed fluxes. We adopted a simple geometric cube box model consisting of a uniform, homogeneous population of electrons described by either a power-law or a thermal energy distribution. The emitting plasma was parameterized by a characteristic size L, number density of electrons n_e, magnetic field strength B, and magnetic field angle ϕ. A power-law index δ and the electron temperature T_e define the power-law and thermal regions, respectively. We reconstructed model Stokes I and V fluxes by summing and differencing the model's O- and X-mode emission, respectively. As noted earlier, this assumes that the propagation angle is not too close to the magnetic field perpendicular direction (Equation 4).

Given these simplifying assumptions, the derived physical parameters should be interpreted as volume-averaged values, whereas actual values could (and almost certainly do) vary significantly within the emitting plasma.

In order to test whether a thermal GS component was present in the observed spectra, we fit two types of models: a pure power-law model and a hybrid model comprising the sum of a power-law region and a separate thermal region. For each star, we fit both power-law and hybrid models, and then calculated the Bayesian Information Criterion (BIC) to evaluate whether the addition of a second thermal component was statistically justified.

Table 1. Star Physical Properties, Observing Log, and Priors

Star	Sp. Type	Class	Distance[a] [pc]	Epoch	UT Range	Prior values					
						Size [$R_\odot$]	Ref.[b]	L_X [10^{30} erg s^{-1}]	Ref.[c]	B [kG]	Ref.[d]
HR 1099	K1IV+G5V	RS CVn	29.6	02 Oct 2013	02:30 – 12:30	7.2	1	13	4	0.2	6
UX Arietis	K0IV+G5V	RS CVn	50.5	24 Dec 2013	02:30 – 12:30	6.5	2	17	4	–	–
Algol	K0IV+B8V	Algol	27.6	29 Sep 2013	10:07 – 12:08	(7.2)[e]	3	13	4	–	–
V410 Tau	K2	WTTS	128.7	08 Jan 2014	06:07 – 11:36	–	–	3.8	5	1.9	7
HD 283572	G5IV	WTTS	125.5	07 Jan 2014	05:33 – 07:33	–	–	12	5	–	–

[a] Distances are from the SIMBAD database (Wenger et al. 2000).
[b] Size references: (1) Abbuhl & Mutel (in prep.), (2) Peterson et al. (2011), (3) Peterson et al. (2010)
[c] X-ray luminosity references: (4) Ness et al. (2002), (5) Telleschi et al. (2007)
[d] Magnetic field references: (6) Donati (1999), (7) Carroll et al. (2012)
[e] The prior for each lobe of the Algol model was half this value. See subsubsection 5.1.3 for model details.

4.1 Bayesian Inference

Since the number of independent data points for each star (10 to 12) is not much larger than the number of free parameters in the model (5 for power-law or 10 for hybrid models), the fitted parameters may be degenerate, which we would like to fully characterize. In addition, we would like to incorporate constraints on parameter values from previous observations, such as radio sizes from VLBI, X-ray luminosities, and magnetic field measurements from ZDI.

Bayesian inference is a natural choice here. First, although we cannot avoid degeneracies, we can better characterize them by numerically sampling the posterior distribution to determine the joint probability density of each parameter pair. Second, priors can naturally include information about parameter constraints from previously-published studies. Third, the Bayesian Information Criterion (BIC) can be used to provide a metric for comparing models with different numbers of parameters, a critical test to evaluate whether the addition of a thermal component is statistically justified.

We implement a constraint on index of refraction n on all the stars. Any plausible model must be free-space accessible (n is real) across all the observed frequencies. To avoid using a prior, we integrate this constraint into the model. We take the product of the emergent flux from the model with a Heaviside function evaluated on n at the observed frequencies. In the case of imaginary n, the emission at that frequency is zero, and the likelihood function will evaluate that model as a poor fit. When we generated preliminary models of V410 Tau and HD 283572, n was imaginary up to the lowest observed frequency at 15 GHz. To counteract this non-physical edge case, we required that n remain real as low as 3 GHz as not to exclude the possibility of flux detected from these two stars in the Very Large Array Sky Survey from the same emitting plasma (Gordon et al. 2021; Lacy et al. 2020).

Stars with previous measurements of the plasma parameters via an independent method have a prior implemented unique to the star. The values we selected are detailed in Table 1. In all cases, the prior probability distribution function was a Gaussian centered on the value with a 20 per cent width. The parameters include:

(1) Characteristic size: For the three close active binaries, VLBI measurements were available to constrain the characteristic size L of the power-law region. The Algol dual-lobe total extent was reported as 7.2 $R_\odot$, so we enforced a Gaussian prior of 20 per cent width centered at half that value for each power-law region in the Algol model (see subsubsection 5.1.3 for model details).
(2) Thermal plasma X-ray emission: We approximate the X-ray luminosity L_X of a hot ($T_e \gg 1$ keV) hydrogen plasma by determining the integrated bremsstrahlung (free-free continuum emission) for a uniform cube with side $L_{\rm box}$ (e.g., Karzas & Latter 1961, equation 26, recast):

$$P_{\rm Br} = 1.5\times10^{29}\cdot\left[\frac{n_e}{10^{10}cm^{-3}}\right]^2\cdot\left[\frac{T_e}{10^7{\rm K}}\right]^{0.5}\cdot\left[\frac{L_{\rm box}}{{\rm R}_\odot}\right]^3 {\rm erg\ sec^{-1}} \quad (6)$$

where n_e and T_e are the number density [cm^{-3}] and electron temperature [K] of the thermal population. We can compare the expected X-ray luminosity of the thermal plasma model with existing estimations.
(3) Magnetic field strength: A six-year Zeeman-Doppler imaging (ZDI) campaign of HR 1099 demonstrated an average field of $\sim$ 0.2 kG. ZDI of V410 Tau measured a magnetic topology dominated by a large-scale bipolar field near the visible pole at $\sim$ 1.9 kG. This value is within expectations for a large-scale field over the magnetospheric cavity of a T-Tauri star (Hartmann et al. 2016). We use this value as the center of the prior for the thermal electron population.

4.2 Fitting procedure

To determine an optimized model for each target, we followed a six step process:

(1) Initialize a model by selecting either a pure power-law electron population or the sum of a power-law and a non-cospatial hot thermal region with parameters informed by literature-reported values (see Table 1).
(2) Search for best-fitting parameter values using a downhill simplex algorithm (Nelder-Mead) to minimize a weighted χ^2 objective function. The `Python` package `lmfit` (Newville et al. 2014) was used for this step.
(3) Initialize the relevant priors (characteristic size, X-ray temperature, magnetic field measurements) for the selected model and target.
(4) Invoke Bayesian inference via Markov Chain Monte Carlo (MCMC) sampling using `Python` package `emcee` (Foreman-Mackey et al. 2013) to determine best-fitting parameter values and associated uncertainty probability distribution functions.
(5) Test for walker convergence (see Appendix B for details):
- Determine the 'goodness-of-chain' by investigating the

Table 2. Observed Stokes Flux Densities

Star	Stokes	15 GHz	23 GHz	31 GHz	35 GHz	41 GHz	45 GHz
HR 1099	I	20.90 ± 0.09	14.66 ± 0.10	9.99 ± 0.09	8.84 ± 0.06	7.26 ± 0.08	6.41 ± 0.07
	V	6.55 ± 0.04	5.05 ± 0.04	3.04 ± 0.03	2.52 ± 0.03	2.00 ± 0.05	1.63 ±0.05
UX Arietis	I	78.82 ± 0.29	57.44 ±0 .17	43.62 ± 0.17	38.79 ± 0.12	30.72 ± 0.22	31.13 ± 0.17
	V	-11.98 ± 0.05	-8.33 ± 0.03	-4.81 ± 0.04	-3.84 ± 0.03	‡	-2.32 ± 0.05
Algol	I	41.83 ±0.18	32.82 ± 0.16	25.98 ± 0.19	25.63 ± 0.13	23.97 ± 0.22	‡
	V	-0.32 ± 0.07	-0.48 ± 0.03	-0.49± 0.04	-0.75 ± 0.06	-0.500 ± 0.07	‡
V410 Tau	I	1.27 ± 0.03	1.28 ± 0.02	1.11 ± 0.03	1.08 ± 0.02	0.80 ± 0.03	0.76 ± 0.04
	V	-0.11 ± 0.02	-0.13 ± 0.01	-0.14 ± 0.02	-0.17 ± 0.02	-0.19 ± 0.02	-0.23 ± 0.03
HD 283572	I	2.29 ± 0.02	1.89 ± 0.02	1.44 ± 0.03	1.13 ± 0.02	0.97 ± 0.03	0.82 ± 0.04
	V	0.27 ± 0.04	0.24 ± 0.04	0.27 ± 0.03	0.24 ± 0.03	0.28 ± 0.05	0.21 ± 0.05

NOTE – All fluxes are in mJy. ‡ indicates missing observation.

walker acceptance fraction and the total number of steps compared to the MCMC auto-correlation time as a function of step-index.

- Adjust the step number or the stretch step parameter and re-run the chain as necessary.

(6) Compare BICs for pure power-law versus hybrid models with separate power-law and thermal components to determine whether the addition of a thermal component is statistically justified.

We modeled the observed SEDs using both power-law and thermal GS emission models in non-cospatial regions, except for Algol. In this case, we considered two oppositely polarized power-law emission regions based on previous VLBI maps of Algol (Mutel et al. 1998; see subsubsection 5.1.3). The fitting procedure began by applying a downhill simplex algorithm with a χ^2 objective function. The resulting best-fit model was used as a starting point for initializing the Bayesian MCMC analysis. Priors for the VLBI sizes, X-ray luminosity, and magnetic field were set based on literature-reported values as listed in Table 1, and any others were set to default prior settings (see Appendix A for the default priors and a discussion of the implementation of probability distribution functions). The objective likelihood function was the residual sum of squares between the model and observed fluxes weighted by their uncertainties.

For each MCMC calculation, we initialized 100 walkers in a small (1 per cent of parameter values) Gaussian hypervolume around the minimized solution. Our step proposal density function was the 'stretch-step' algorithm (Goodman & Weare 2010), a variable step-length algorithm designed to quickly fill posterior space by scaling step sizes with the distribution of walkers. For all runs, a period of tracked 'burn-in' steps gave the walkers time to undergo this filling process.

To determine if the walkers had converged, we evaluate the 'goodness-of-chain' of the MCMC run based on the walker acceptance fraction and the auto-correlation time compared to the total step number. For chains with acceptance fractions below 0.1 or above 0.5, the average step length was shortened or lengthened, respectively, with a target acceptance fraction of 0.23 (Gelman et al. 1997). We define convergence of the chain as the total number of steps exceeding 50 times the auto-correlation time of the chain as estimated by `emcee`. We increased the length until the chain met this criterion. See Appendix B for an extended discussion of evaluating the goodness-of-chain.

4.3 Testing the Thermal GS Hypothesis: Bayes Information Criterion

Since a primary focus of this research was to determine whether thermal GS radiation is detectable in the observed SEDs, we need to evaluate whether the addition of a thermal GS component to the emission model is statistically justified. To do this, we use the Bayesian Information Criterion (BIC), defined as:

$$\mathrm{BIC} = k\ln(n) - 2\ln(\hat{L}) \tag{7}$$

where k is the number of parameters estimated by the model, n is the number of data points in the observations, and $\hat{L}$ is the maximized value of the likelihood for that particular model, i.e., $\hat{L} = p(x|\hat{\theta}, M)$ where $\hat{\theta}$ are the parameters that maximize the likelihood and x is the observed data (Schwarz 1978). The BIC can be used to select the model that fits the data with a minimum number of free parameters by penalizing model complexity (i.e., the number of parameters in the model (Liddle 2007)).

For each star, we evaluated the BIC for a pure power-law model, and for the hybrid model i.e., the sum of a power-law and thermal GS emission. Although the actual BIC value depends on the particular values of n, k, and $\hat{L}$ for that model, the key metric is the difference in BIC values between two models,

$$\Delta\mathrm{BIC} = \mathrm{BIC}_{\mathrm{pwr+th}} - \mathrm{BIC}_{\mathrm{pwr}} \tag{8}$$

where $\Delta\mathrm{BIC} < 0$ indicates that the inclusion of the additional free parameters supports the model with the lower BIC. ΔBICs between -2 and -6 are considered 'positive' evidence for the more complex model, whereas a difference between -6 and -10 constitutes 'strong' evidence, and $Delta$BICs beyond this are 'very strong' evidence (Bauldry 2015).

We find that the three close binaries (Algol, HR 1099, UX Arietis) have large positive ΔBICs. indicating that a simple power-law model is adequate, whereas the two pre-main-sequence stars (V410 Tau, HD 283572) have large negative ΔBICs, indicating that the more complex hybrid model is favored. The ΔBICs for all stars are listed in Table 3.

5 RESULTS

Here we summarize the results of the fitting procedure for each star. We compare best-fit model plasma parameters (magnetic field, electron density, source size etc.) with estimates from previous studies using other techniques. However, for all five stars the joint posterior model parameter probability distributions (Figure 4, 5, 7, and 8)

Table 3. Best-fitting Model Parameters

Star	Power-law component					Thermal component					Selection Metric[a]
	L [$R_\odot$]	δ	log n_e [cm^{-3}]	B [G]	ϕ [deg]	L [$R_\odot$]	log T [MK]	log n_e [cm^{-3}]	B [G]	ϕ [deg]	ΔBIC
HR 1099	2.6	3.1	6.6	240	122°	–	–	–	–	–	8.6
UX Arietis	7.8	2.7	5.7	180	85°	–	–	–	–	–	11.8
Algol	3.4	2.1	4.7	170	(54°, 146°)[b]	–	–	–	–	–	–
V410 Tau	1.2	2.9	8.1	94	67°	0.9	7.9	10.5	1860	28°	−15.7
HD 283572	2.6	3.6	8.6	110	110°	0.6	8.6	10.9	740	157°	−21.2

NOTE – Parameter uncertainties are not listed in this table. They are best characterized by the joint posterior model parameter probability distribution shown in Figure 4 for HR 1099 and UX Arietis, Figure 5 for Algol, Figure 7 for V410 Tau, and Figure 8 for HD 283572. The listed model parameters are the median values of the MCMC sampling.

[a] The selection metric is defined as difference between the Bayesian Information Criteria of the power-law GS model and the hybrid (power-law plus thermal GS) model.

[b] The Algol model requires two angles that parametrize the two oppositely circularly polarized emission lobes. See subsubsection 5.1.3 for the model details.

are strongly pairwise degenerate in at least some parameters. Hence, the parameter uncertainties, as shown in the parameter distribution functions about the median value, are relatively large.

Our main focus is to establish whether a pure power-law emission model alone or a hybrid model with a thermal GS component is required to fit the observed SEDs. To this end, we calculate the BIC difference for both models. As described above, this difference is a quantitative measure of the viability of the more complex hybrid model for each star.

5.1 Active close binaries

5.1.1 HR 1099

HR 1099 is a well-known active close binary with extensive studies at radio, UV, and X-ray wavelengths. It was one of the earliest targets of Zeeman-Doppler Imaging (ZDI) investigations that found a $\sim$ 200 G magnetic field (Donati 1999). The Rapid ASKAP Continuum Survey recently detected $V/I \sim -16$ per cent at 888 MHz (Pritchard et al. 2021).

A pure power-law model fits the observed SEDs quite well as shown in Figure 3 and supported by the ΔBIC value in Table 3. The magnetic field of $B = 240$ G agrees with the prior. The model predicts a flip to a negative Stokes V below $\sim$ 10 GHz, which also agrees with the 888 MHz detection. The size of $L = 2.5\,R_\odot$, deviates strongly from the flaring size prior we implemented of 6.5 $R_\odot$, but agrees with the upper limit $L < 5R_\odot$ from VLBI at 22 GHz (Abbuhl & Mutel, in prep.) during quiescence.

5.1.2 UX Arietis

UX Arietis is another well-studied star for its flares in the radio and X-ray. Radio flares on have demonstrated magnetic field strengths exceeding a kG (Torricelli-Ciamponi et al. 1998), while X-ray flares indicate peak temperatures of 100MK (Livshits et al. 2003). Measurement of the quiescent radio emission has produced magnetic field estimates on the order of 100G (Donati et al. 1992). Notably, Chiuderi Drago & Franciosini (1993) theorize that a thermal electron distribution could explain the 6 cm quiescent emission component and determine a pure-thermal model with a constant magnetic field is unlikely to explain the observed fluxes.

The fit to the SED in Figure 3 and the resulting ΔBIC support the simpler pure power-law model. The magnetic field of 180 G agrees with the previously mentioned measurements, and $\delta = 2.7$ also agrees with the prediction of Chiuderi Drago & Franciosini (1993). The best-fitting value for the size of 7.8 $R_\odot$ slightly exceeds that of the VLBI measurements of 6.5 $R_\odot$. The uncertainties are quite narrow and the best-fitting solution returned by `lmfit` is outside of the contours, indicating `emcee` found a better solution under the priors.

5.1.3 Algol

Algol has demonstrated strong coronal radio emission. This system has a typical flare B-field of 250 G and energetic electron densities of 10^3 to 10^5 cm^{-3} (Mutel et al. 1998). X-ray measurements of a flare have shown a hot component of up to 40 MK (Yang et al. 2011).

VLBI measurements of Algol have indicated the presence of two significant lobes of radio emission with opposite polarization helicity (Peterson et al. 2010). We choose to model this by allowing the magnetic field angle with respect to the observer for each region to vary independently of each other (ϕ and ϕ_2). In the model, the angles are initialized exactly orthogonal to each other but not constrained to remain orthogonal to account for slight deviations from net zero circular polarization.

Since the Algol model requires a six-parameter model for each component and we only observed at five frequencies, attempting to fit with the added thermal component would result in no remaining degrees of freedom. Due to this, we are unable to definitively conclude that a thermal population is not necessary to explain the Algol SED. The Stokes I plot tends to show a slight rise in flux in the 30–40 GHz range that may be consistent with a secondary component. However, further observations are necessary to make this determination.

The resulting individual parameter values agree well with previous measurements. The size of each lobe of L=2.9 $R_\odot$ is approximately half of the total size of the total size of the two oppositely polarized lobes, as expected. The joint posterior model parameter probability distributions in Figure 5 demonstrate strong degeneracy. More simultaneous multi-frequency observations of the Algol system are necessary to characterize the nature of the radio emission mechanisms.

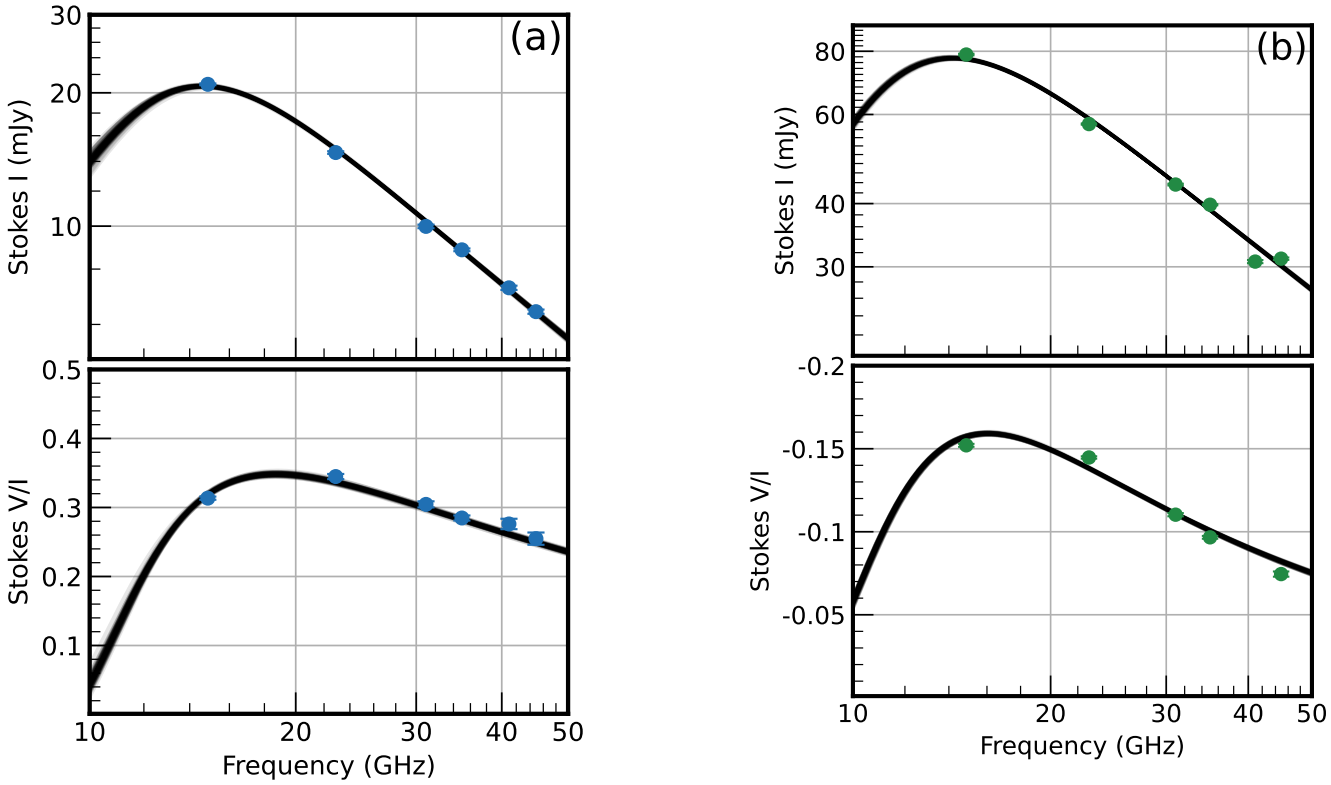

(a) HR 1099

(b) UX Arietis

Figure 3. Observed spectral energy distributions for the close active binaries HR 1099 and UX Arietis between 15 GHz and 45 GHz. The best-fitting model SEDs plotted in black are generated from 100 randomly selected walker positions in the final 10 per cent of the MCMC run. Best-fitting plasma parameters are listed in Table 3.

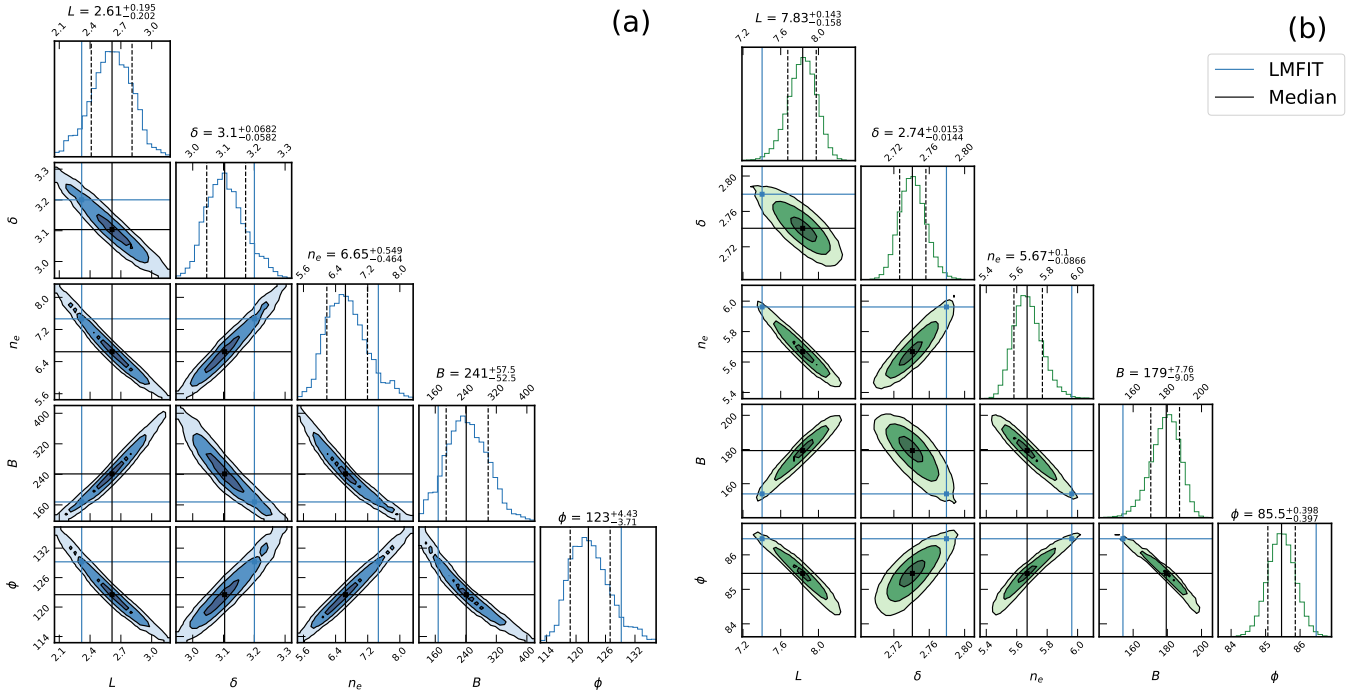

(a) HR 1099

(b) UX Arietis

Figure 4. Joint posterior model parameter probability distributions for power-law electron distribution GS emission model fitted to SED of HR 1099 and UX Arietis. Note that most parameters are highly correlated, so unique values are degenerate. Contour levels are shown at 39, 87, and 99 per cent.

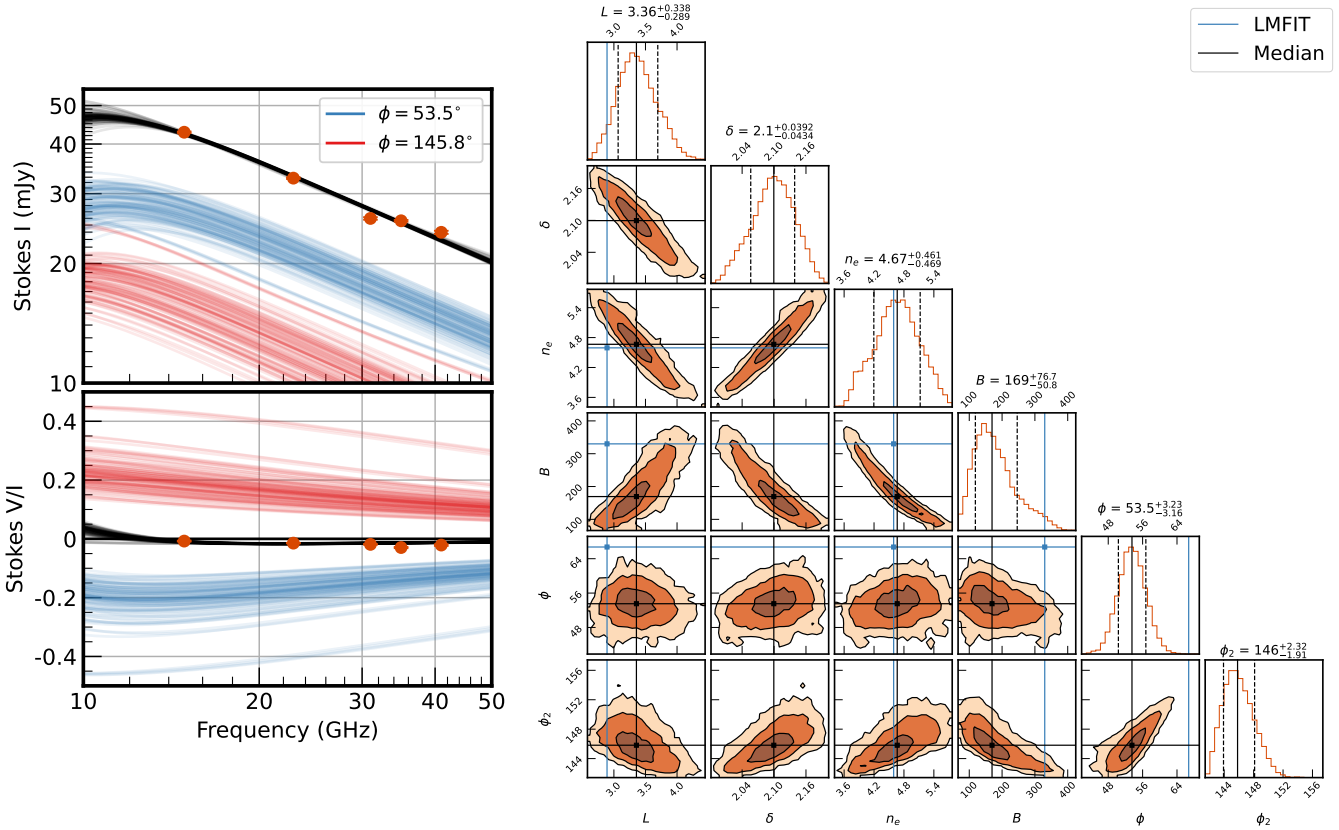

Figure 5. Observed spectral energy distribution and joint posterior model parameter probability distributions for the sum of two power-law electron distribution GS emission models fitted to the SED of Algol (see subsubsection 5.1.3 for model details). The best-fitting models are plotted in black as the sum of the emission from each individual component specified by their angle, plotted in blue and red. The parameters to produce these models are generated from 100 randomly selected walker positions in the final 10 per cent of the MCMC run. Note that the low polarization is due to the opposite helicity of the two power-law regions. Best-fitting parameters are listed in Table 3. Contour levels are shown at 39, 87, and 99 per cent.

5.2 Weak T-Tauris

5.2.1 V410 Tau

V410 Tau is a weak-lined T-Tauri star in the nearby Taurus star formation region and was one of the first stars to show evidence for strong magnetic fields via Zeeman-Doppler imaging (Donati et al. 1997). Since then, follow-up analyses of archival observations identified large scale dipolar magnetic fields strengths of nearly ~ 2 kG (Carroll et al. 2012). X-ray observations have suggested a quiescent coronal temperature of 20 MK and peak flare temperatures exceeding 40 MK (Telleschi et al. 2007). Following the epoch of our observations, long-term studies have suggested a magnetic cycle exceeding eight years (Yu et al. 2019), or perhaps a stellar spot cycle of ~15 years based on long-term trends in the light curve of the star as it rotates with a 1.87 d period (Hambálek et al. 2019). A recent spectropolarimetric monitoring campaign has also constrained the magnetic field topology, but the strong toroidal component of nearly 400 G that was uncovered remains to be explained in the absence of an observable disk (Finociety et al. 2021).

We find a ΔBIC = -15.7. This is strong evidence that the thermal component is required to explain the observed SED, clearly seen from an inspection of the plot in Figure 6. The X-ray luminosity as calculated using Equation 6 and the best-fitting parameters gives $L_X = 3.7\times10^{30}$ erg/s, in good agreement with Telleschi et al. (2007), despite a best-fitting logT = 7.9, about 0.5 dex higher than indicated by the X-ray data. The magnetic field reported by Carroll et al. (2012) is also in agreement with the model value of 1860 G for the thermal region.

The joint posterior model parameter probability distributions in Figure 7 show strong degeneracy in the parameters that define each region. However, there is little correlation across the power-law and thermal populations. The thermal region tends to be more well-defined than the power-law population, likely due to the relatively strong priors on the X-ray luminosity and the magnetic field strength.

5.2.2 HD 283572

HD 283572 is one of the brightest X-ray sources in the Taurus star-formation region at $L_X = 1.2 \times 10^{31}$ erg s^{-1}. HD 283572 has been shown to have X-ray flares consistent with B-fields of 300-500 G (Favata et al. 2001). X-ray measurements of quiescent emission indicate coronal temperatures of 19-26 MK (Franciosini et al. 2007). Similar to V410 Tau, there is not an observable disk (Sullivan & Kraus 2022).

We find ΔBIC = -21.2, providing very strong evidence for the added thermal population. Our best-fitting solution agrees almost precisely with the X-ray luminosity, returning a value of $L_X = 1.15\times 10^{31}$ erg s^{-1}, as expected due to the prior. Like V410 Tau, this is despite a significant difference in the best-fitting temperatures. The magnetic field also agrees well in the thermal region. No quiescent magnetic field measurements are available for comparison to the best-fitting power-law population.

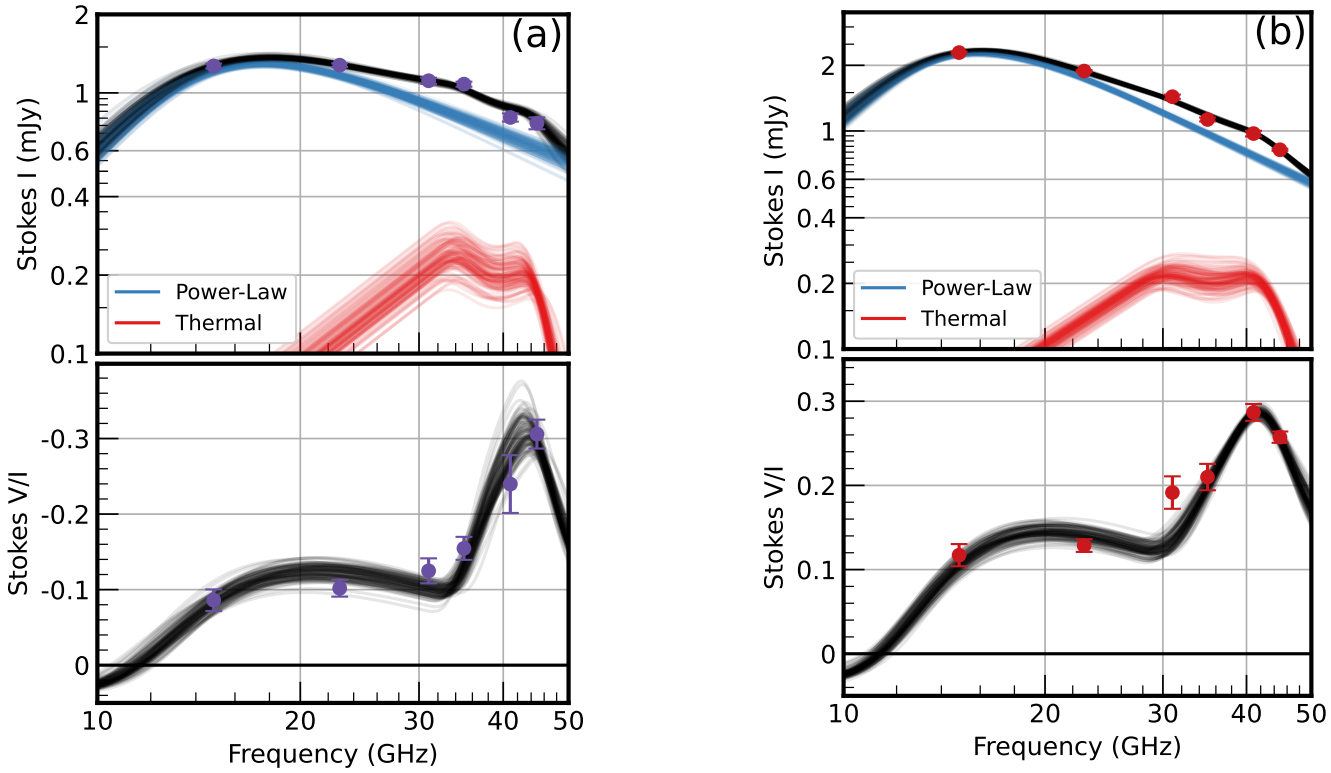

(a) V410 Tau

(b) HD 283572

Figure 6. Observed spectral energy distributions for the pre-main-sequence stars V410 Tau and HD 283572 between 15 GHz and 45 GHz with best-fitting models consisting of separate power-law and hot thermal GS emission models. The best-fitting models plotted in black are generated from 100 randomly selected walker positions in the final 10 per cent of the MCMC run. Best-fitting plasma parameters are listed in Table 3.

The correlations across the regions are relatively small, as seen in Figure 8. The errors are more extensive in the power-law region compared to the thermal population parameters. Since the X-ray luminosity agrees so well, this is likely the driving constraint on the parameters that define the thermal GS emission.

6 DISCUSSION

A pure power-law model is the obvious choice for the RS CVn stars. The resulting best-fitting parameters from Bayesian inference also produce results consistent with previously reported values. However, the MCMC sampling analysis also uncovered a strong degeneracy across parameters. Future work in breaking this degeneracy for active close binaries can be done by employing radio observations accompanied by contemporaneous, independent measurements, such as ZDI to measure magnetic fields or X-ray observations to find emission measures.

The dual-lobed emission regions with opposite polarization holicity complicate the Algol system. Higher spectral and spatial resolution is necessary to determine if a thermal component may be contributing to the SED. Similar to the RS CVn stars, strong degeneracies across the plasma parameters for the two identical, oppositely polarized power-law populations make determining the specific values challenging without independent measurements. With the added complication of a rapid orbital period and a complex coronal structure throughout the entire phase, further observations are necessary to probe the properties of the radio emission from this system.

The best-fitting solutions for the two models of both pre-main-sequence stars return values of the BIC that strongly favor the addition of a thermal component to explain the rising fractional polarization at the upper frequencies of the SEDs. We can conclude that a thermal distribution of electrons emitting GS radiation may explain a component of the SEDs of these stars.

Notably, the shared plasma parameters are very different for V410 Tau and HD 283572. The thermal regions tend to be much smaller volumes but nearly hundreds of times denser than the power-law population. Additionally, the best-fitting magnetic field strength and angle are very different in both cases. The thermal region is best modeled by a field of about an order of magnitude larger at an angle well outside the reported uncertainty of the MCMC sampling. These differences indicate that these two plasma populations are not co-spatial.

These results for both WTTs–in combination with the lack of evidence of a thermal component in the other target populations–allow us to speculate that the former presence of a detectable accretion disc may be responsible for generating the thermal component. Previous modeling work (Waterfall et al. 2019) indicates that even weak T-Tauri stars that lack an observable disk–such as V410 Tau (Yu et al. 2019; Finociety et al. 2021) and HD 283572 (Sullivan & Kraus 2022)–tend to demonstrate similar magnetic behavior as their classical counterparts. Gómez de Castro & Marcos-Arenal (2012) have proposed a magnetospheric geometry of T-Tauri stars where magnetic shearing and reconnection events on the inner edge of the disc are possible due to a mismatch in the rotation rates of the stellar surface and the inner disc. For an extended discussion of accretion

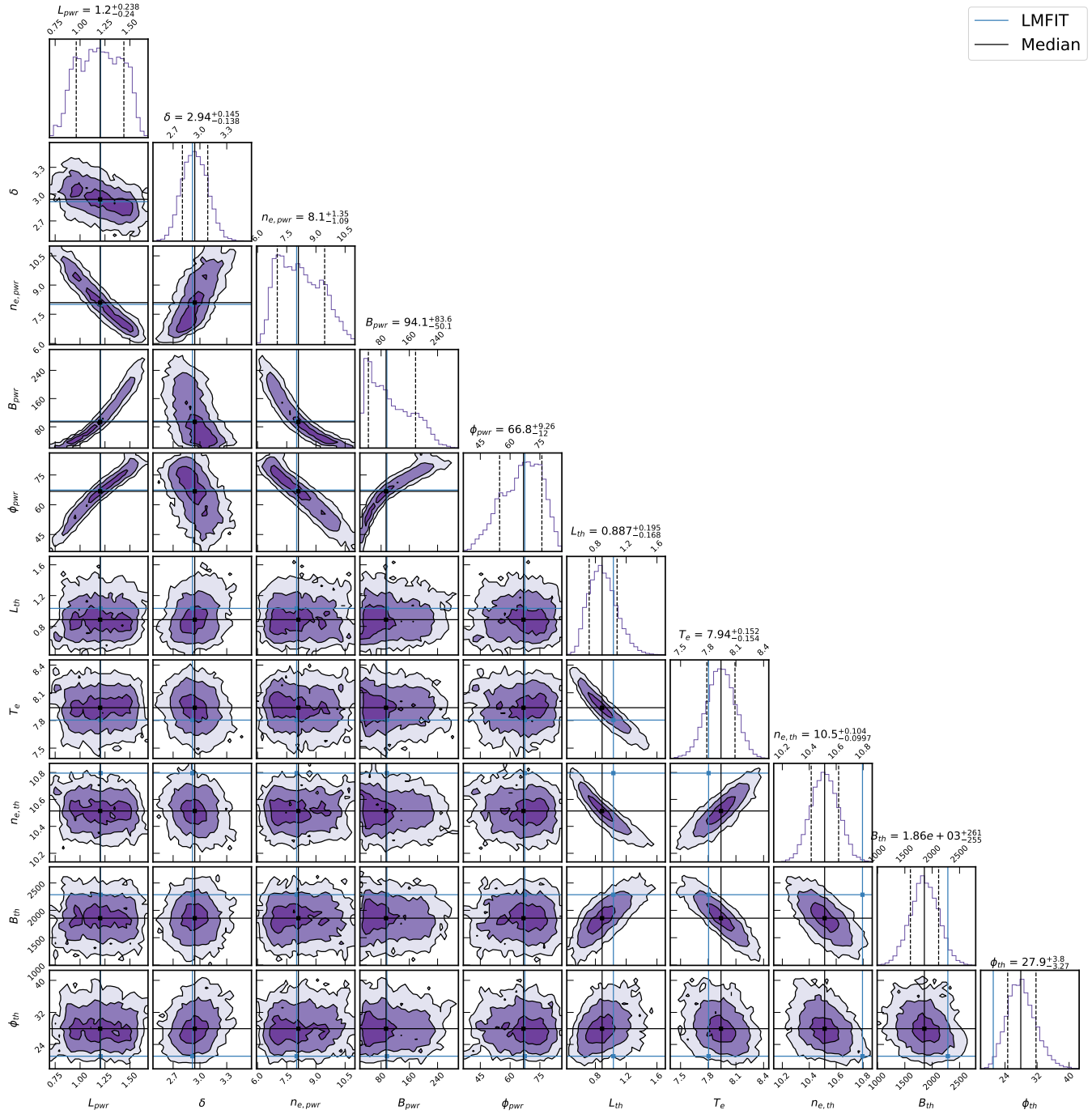

Figure 7. Joint posterior model parameter probability distributions for power-law electron distribution GS emission model fitted to SED of V410 Tau. Correlations across the separate regions are much weaker compared to the degeneracies within the parameters that define each region. Note the general disagreement of the least squares result with nearly all of the thermal population plasma parameters. Contour levels are shown at 39, 87, and 99 per cent.

processes in T-Tauri stars, see Hartmann et al. (2016) and references therein.

Within this framework, Figure 9 illustrates a potential model for the spatial distribution of different electron populations. Due to strong coronal magnetic field activity, a halo of power-law electrons surrounds the star. Meanwhile, the thermal emission comes from the star-disc shearing region on the inner edge of the disc, where magnetic reconnection events accelerate high densities of thermal electrons to semi-relativistic speeds in a smaller volume.

Note that this speculative model is not incompatible with the picture of the HD 283572 flare analysis in Favata et al. (2001). They argue that large coronal loops spanning the distance between the star and the disc are not responsible for the observed X-ray flares. Our model proposes only that the thermal emission is responsible for the X-rays and the thermal GS component most likely originates from the inner edge of the disc, not between the disc and the star. Additionally, without X-ray observations contemporaneous to our observing epoch, it is unknown whether a flare was occurring, and

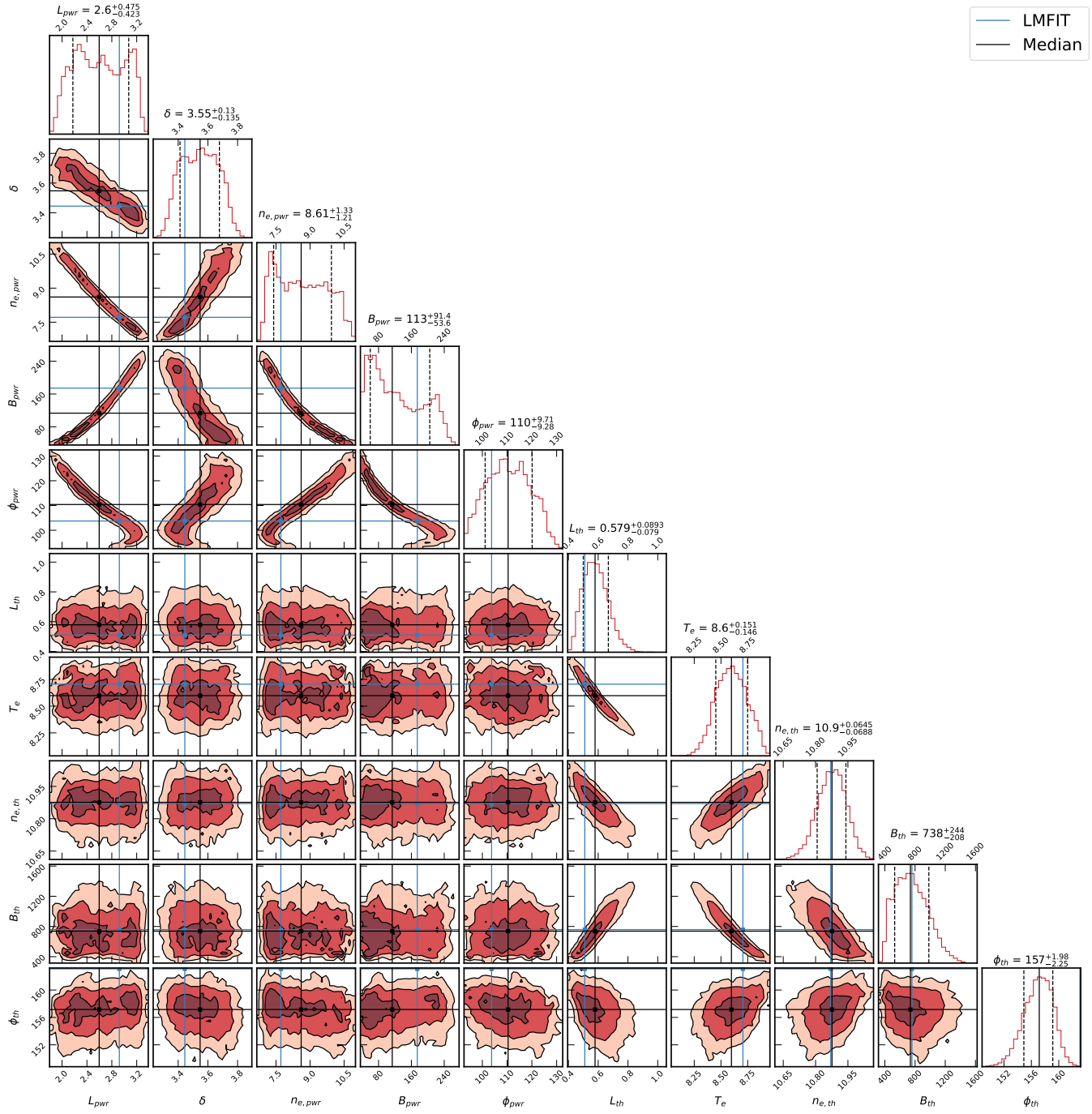

Figure 8. Joint posterior model parameter probability distributions for power-law electron distribution GS emission model fitted to SED of HD 283572. Note the turnover in the direction of the correlations in $\phi_{\rm pwr}$. This effect is likely due to the approach of a line-of-sight nearly orthogonal to the B-field and thus the condition of Equation 4 is not met. Contour levels are shown at 39, 87, and 99 per cent.

somewhat more likely that quiescent emission due to constant star-disc shearing action is driving the production of semi-relativistic thermal electrons. These electrons would also explain the significant quiescent X-ray luminosity given our prediction of L_X, calculated from the best-fitting model parameters for HD 283572.

7 SUMMARY

In this work, we report on multi-frequency observations of five radio-loud stars. In combination with prior X-ray, ZDI, and VLBI measurements (where available), we characterize the emission of these stars with simple models of a uniform, homogenous plasma with either a power-law or thermal energy distribution. We use Bayesian inference to describe the correlations between the model parameters and determine if a thermal population in addition to the standard power-law distribution can be justified.

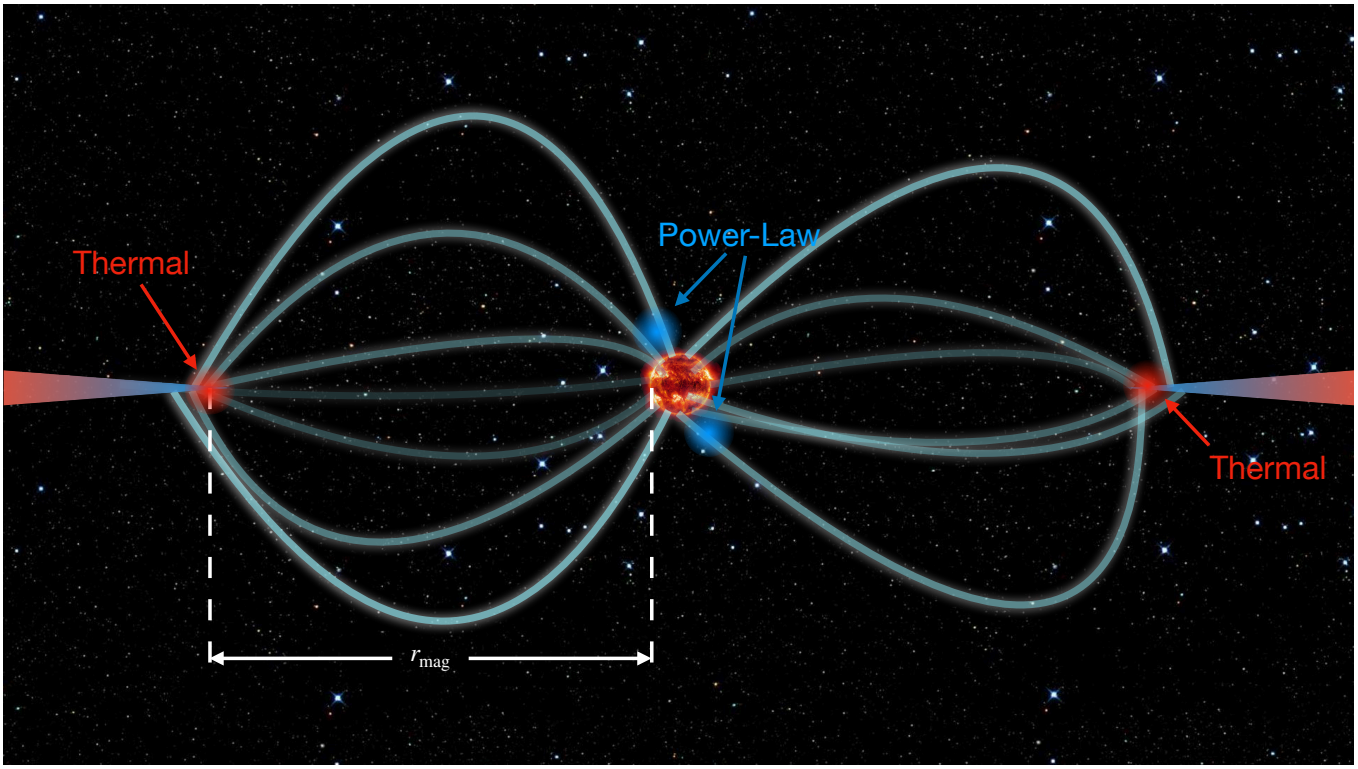

Figure 9. Conjectural locations of power-law (blue circles) and thermal (red circles) GS emission regions from the pre-main-sequence objects HD 283572 and V410 Tau. The separation $r_{\rm mag}$ is the radius of the magnetospheric cavity. This figure is adapted from Gómez de Castro & Marcos-Arenal (2012).

For the two RS CVn stars HR 1099 and UX Arietis, we find that the SED can be well-described by the pure power-law model, and all parameters are well-constrained. However, MCMC sampling revealed strong degeneracy across the model parameters. Breaking this degeneracy will require contemporaneous, independent determinations of multiple plasma parameters.

Algol is moderately well-modeled by two identical lobes of opposite polarization helicity. Due to the added parameter required for generating such a model, determination of the potential of a thermal component was not possible with these observations. Higher spectral and spatial density observations are necessary to investigate the potential for thermal GS in Algol and similar systems.

The weak T-Tauri stars (V410 Tau and HD 283572) were best described by a hybrid power-law plus thermal GS emission model. We speculate that the disc may be responsible for this thermal emission, where star-disc magnetic shearing and re-connection events drive the acceleration of dense thermal electrons to semi-relativistic speeds. With the identification of pre-main-sequence stars as a potential source of thermal GS emission, further investigation into other systems with different stellar types and higher spectral and spatial resolution observations are required to characterize this emission mechanism.

ACKNOWLEDGEMENTS

This work made use of data taken by the Karl G. Janksy Very Large Array. The National Radio Astronomy Observatory is a facility of the National Science Foundation operated under cooperative agreement by Associated Universities, Inc. This research made use of the `lmfit` non-linear least-squares minimization `Python` library (Newville et al. 2014), and `astropy`, a community developed core `Python` package for astronomy (The Astropy Collaboration 2018). We also made use of `emcee`, an MIT licensed pure-`Python` implementation of the affine invariant Markov Chain Monte Carlo ensemble sampler (Foreman-Mackey et al. 2013). We also used the `Python` module `corner.py` to visualize multidimensional results of Markov Chain Monte Carlo simulations (Foreman-Mackey 2016). This research has made use of the SIMBAD database, operated at CDS, Strasbourg, France (Wenger et al. 2000). The authors acknowledge Weaver et al. (2021) for the inspiration to provide all code used to generate figures.

DATA AVAILABILITY

We have provided Table 2 as our observed Stokes I and V flux densities. Visibilities are available for download from the National Radio Astronomy Observatory Data Archive. The saved MCMC sampling runs are available on request from the corresponding author. The latest version of the code used to generate each figure is hosted on the Github repository for this project. An archival release of the code coincident with publication is also hosted on Zenodo doi:10.5281/zenodo.7222487.

REFERENCES

Bastian T. S., Benz A. O., Gary D. E., 1998, Annual Review of Astronomy and Astrophysics, 36, 131

Bauldry S., 2015, in Wright J. D., ed., , International Encyclopedia of the Social and Behavioral Sciences (Second Edition), second edition edn, Elsevier, Oxford, pp 615–620, doi:https://doi.org/10.1016/B978-0-08-097086-8.44055-9, `https://www.sciencedirect.com/science/article/pii/B9780080970868440559`

Carroll T. A., Strassmeier K. G., Rice J. B., Künstler A., 2012, A&A, 548, A95
Chiuderi Drago F., Franciosini E., 1993, ApJ, 410, 301
Donati J. F., 1999, MNRAS, 302, 457
Donati J. F., Semel M., 1990, Solar Physics, 128, 227
Donati J. F., Semel M., Rees D. E., 1992, A&A, 265, 669
Donati J. F., Semel M., Carter B. D., Rees D. E., Collier Cameron A., 1997, MNRAS, 291, 658
Drake S. A., Simon T., Linsky J. L., 1992, ApJS, 82, 311
Dulk G. A., 1985, ARA&A, 23, 169
Dulk G. A., Melrose D. B., White S. M., 1979, ApJ, 234, 1137
Favata F., Micela G., Reale F., 2001, A&A, 375, 485
Finociety B., et al., 2021, MNRAS, 508, 3427
Foreman-Mackey D., 2016, The Journal of Open Source Software, 1, 24
Foreman-Mackey D., Hogg D. W., Lang D., Goodman J., 2013, PASP, 125, 306
Franciosini E., et al., 2007, A&A, 468, 485
García-Sánchez J., Paredes J. M., Ribó M., 2003, Astronomy & Astrophysics, 403, 613
Gelman A., Gilks W. R., Roberts G. O., 1997, The Annals of Applied Probability, 7, 110
Gelman A., Meng X.-L., Brooks S., Jones G. L., 2011, Handbook of markov chain Monte Carlo. CRC Press (Taylor Francis Group)
Goodman J., Weare J., 2010, Communications in Applied Mathematics and Computational Science, 5, 65
Gordon Y. A., et al., 2021, ApJS, 255, 30
Gómez de Castro A. I., Marcos-Arenal P., 2012, ApJ, 749, 190
Hambálek L., Vaňko M., Paunzen E., Smalley B., 2019, MNRAS, 483, 1642
Hartmann L., Herczeg G., Calvet N., 2016, Annual Review of Astronomy and Astrophysics, 54, 135
Karzas W. J., Latter R., 1961, ApJS, 6, 167
Kobayashi K., et al., 2006, ApJ, 648, 1239
Lacy M., et al., 2020, PASP, 132, 035001
Launhardt R., Loinard L., Dzib S. A., Forbrich J., Bower G. C., Henning T. K., Mioduszewski A. J., Reffert S., 2022, The Astrophysical Journal, 931, 43
Leto P., Trigilio C., Buemi C. S., Umana G., Leone F., 2006, Astronomy and Astrophysics, 458, 831
Leung P. K., Gammie C. F., Noble S. C., 2011, ApJ, 737, 21
Liddle A. R., 2007, MNRAS, 377, L74
Livshits I. M., Livshits M. A., Pallavicini R., 2003, Advances in Space Research, 32, 1181
McMullin J. P., Waters B., Schiebel D., Young W., Golap K., 2007, in Shaw R. A., Hill F., Bell D. J., eds, Astronomical Society of the Pacific Conference Series Vol. 376, Astronomical Data Analysis Software and Systems XVI. p. 127
Mutel R. L., Molnar L. A., Waltman E. B., Ghigo F. D., 1998, ApJ, 507, 371
Ness J. U., Schmitt J. H. M. M., Burwitz V., Mewe R., Raassen A. J. J., van der Meer R. L. J., Predehl P., Brinkman A. C., 2002, A&A, 394, 911
Newville M., Stensitzki T., Allen D. B., Ingargiola A., 2014, LMFIT: Non-Linear Least-Square Minimization and Curve-Fitting for Python, Zenodo, doi:10.5281/zenodo.11813
Nindos A., Kundu M. R., White S. M., Shibasaki K., Gopalswamy N., 2000, ApJS, 130, 485
Osten R. A., Bastian T. S., 2006, ApJ, 637, 1016
Peterson W. M., Mutel R. L., Güdel M., Goss W. M., 2010, Nature, 463, 207
Peterson W. M., Mutel R. L., Lestrade J. F., Güdel M., Goss W. M., 2011, ApJ, 737, 104
Petrosian V., 1981, ApJ, 251, 727
Pritchard J., et al., 2021, MNRAS, 502, 5438
Robinson P. A., Melrose D. B., 1984, Australian Journal of Physics, 37, 675
Schwarz G., 1978, Annals of Statistics, 6, 461
Sokal A. D., 1996, Nuclear Physics B Proceedings Supplements, 47, 172
Storey M. C., Hewitt R. G., 1995, Publ. Astron. Soc. Australia, 12, 174
Sullivan K., Kraus A. L., 2022, ApJ, 928, 134
Tak H., Ghosh S. K., Ellis J. A., 2018, MNRAS, 481, 277
Tan B., 2022, Research in Astronomy and Astrophysics
Telleschi A., Güdel M., Briggs K. R., Audard M., Scelsi L., 2007, A&A, 468, 443
The Astropy Collaboration 2018, astropy v3.1: a core python package for astronomy, Zenodo, doi:10.5281/zenodo.4080996
Torricelli-Ciamponi G., Franciosini E., Massi M., Neidhoefer J., 1998, A&A, 333, 970
Trigilio C., Buemi C. S., Umana G., Rodonò M., Leto P., Beasley A. J., Pagano I., 2001, A&A, 373, 181
Trubnikov B. A., 1958, PhD thesis, Dissertation, Moscow (US-AEC Tech. Inf. Service, AEC-tr-4073 [1960]), (1958)
Umana G., Trigilio C., Hjellming R. M., Catalano S., Rodono M., 1993, A&A, 267, 126
Waterfall C. O. G., Browning P. K., Fuller G. A., Gordovskyy M., 2019, Monthly Notices of the Royal Astronomical Society, 483, 917
Weaver I. C., et al., 2021, AJ, 161, 278
Wenger M., et al., 2000, A&AS, 143, 9
Williams P. K. G., 2018, in Handbook of Exoplanets, Vol. 472, Handbook of Exoplanets. Handbook of Exoplanets, pp 589 – 609, doi:10.1007/978-3-319-55333-7_171, http://link.springer.com/10.1007/978-3-319-55333-7_171
Yang X.-J., Lu F.-J., Aschenbach B., Chen L., 2011, Research in Astronomy and Astrophysics, 11, 457
Yu L., et al., 2019, MNRAS, 489, 5556

APPENDIX A: DEFAULT PRIORS

Careful selection of probability distribution functions (PDFs) to implement priors is necessary to make statistically sound claims from the posterior (Tak et al. 2018). Prior PDFs must be normalizable, even if the explicit normalization is not relevant. The generalized Gaussian and the inverse-gamma function are common options for implementing scientific knowledge in the form of a prior. The generalized Gaussian function is given by:

$$p(x) \propto \exp(-|(x-\mu)/\sigma|^s) \tag{A1}$$

Where μ adjusts the center of the Gaussian, σ modifies the width, and s determines how rapidly the fall-off occurs beyond 1σ. Selecting $s = 2$ is a good choice for previous measurements that include uncertainty, i.e., a standard Gaussian distribution. Larger s can apply boundaries on parameter space where a model is no longer valid. Implementing a lower-bound is best done via the inverse-gamma function, given by:

$$p(x) \propto x^{-a-1}\exp(-b/x) \tag{A2}$$

Where a 'soft' lower limit is given by $\frac{b}{a+1}$ and a and b modify the region around the limit, respectively. This PDF is a good option when parameters have sharp lower cutoffs as an alternative to the Heaviside function, which is not normalizable.

We implemented a default prior PDF if a star did not have prior measurements for a particular parameter. These options are summarized in Table A1. The PDFs selected for δ, ϕ, and T_e are motivated by the validity of the approximate expressions for η_ν and κ_ν in Robinson & Melrose (1984) and Dulk (1985). In the case of the B-field of the power-law region, the expressions are only valid if $\nu/\nu_B > 10$. If $\nu_B = 2.8B$ MHz and the lowest observed frequency is 15 GHz, then we can solve for a maximum B strength of $\sim$ 530 G. Finally, the PDFs applied to L, n_e, and the thermal B prevent drifting into nonphysical negative values.

APPENDIX B: 'GOODNESS-OF-CHAIN'

Auto-correlation analysis is a necessary component of any publication employing MCMC sampling. We first discuss the auto-correlation time as a measure of best-fitting solution convergence, and then we evaluate chain exploration efficiency using the step acceptance fraction.

The auto-correlation time is a useful measure of how well an MCMC run has converged by evaluating whether the chain is independent of its initial position. The Monte Carlo standard error (MCSE) can be found from the variance:

$$\sigma^2 = \frac{\tau_f}{N}\hat{\sigma}_n \tag{B1}$$

Where τ_f is the integrated auto-correlation time for the chain and $\hat{\sigma}_n$ is the variance of the chain. (The familiar ordinary Monte Carlo error of $1/\sqrt{N}$ can be recovered if the chain samples are independent, i.e., $\tau_f = 1$). Thus, an estimation of the auto-correlation time of the chain is a direct measurement of the error.

We stochastically define convergence as if the total length of the chain exceeds 50 times the auto-correlation time. To determine if the chain meets this threshold, the chain is correlated with itself at equal intervals throughout the sampling. MCMC runs that do not meet this threshold have the number of steps increased proportionally. We point the reader to Sokal (1996) and Gelman et al. (2011) for a derivation of MCSE and further discussion of evaluating chain independence.

We may also qualitatively evaluate a chain by plotting the one-dimensional density of each parameter of each walker versus the step number, called a 'walker plot'. An MCMC run that has converged will demonstrate relatively constant density over the same region for the entire chain length. Large-scale trends in the movement of the walkers or diverging densities indicate instability in posterior space. Figure B1 shows an example of a successful MCMC walker plot from the burn-in steps of the run for UX Arietis.

The acceptance fraction quantifies how often a walker 'accepts' a step. It takes a step either due to a preferable value of the posterior or against the posterior gradient. This will occur with a probability proportional to the ratio of the posterior values at the current and proposed location. For optimal speed in characterizing the posterior probability distribution, the acceptance fraction should approach 0.23 (Gelman et al. 1997). For an MCMC chain that implements the 'stretch-step' algorithm, α is a number greater than 2 that parametrizes the possible step lengths, where a walker will step in the direction of another randomly selected walker with uniform probability of lengths between $1/\sqrt{\alpha}$ and $\sqrt{\alpha}$ (Goodman & Weare 2010). Reducing α can generally increase the acceptance fraction (and therefore the average step length), but the auto-correlation time is likely to grow, so a modification of the chain's total length may also be necessary.

The final settings and results of the `emcee` runs used in this work are reported in Table B1. In all cases, we ran chains until the auto-correlation condition was met and the acceptance fraction fell between 0.1 and 0.5.

This paper has been typeset from a TEX/LATEX file prepared by the author.

Table A1. Default Priors

			Generalized Gaussian			Inverse Gamma	
Component	Parameter	Unit	μ	σ	s	a	b
Power-Law	L	[$R_\odot$]	–	–	–	0.1	0.022
	δ		4	2.5	10	–	–
	$\log(n_e)$	[cm^{-3}]	–	–	–	1	2
	B	[G]	265	265	10	–	–
	$\phi_{(1,2)}$	[deg]	90	70	20	–	–
Thermal	L	[$R_\odot$]	–	–	–	0.1	0.022
	$\log(T_e)$[a]	[K]	8	1	10	–	–
	$\log(n_e)$	[cm^{-3}]	–	–	–	1	2
	B	[G]	–	–	–	1	2
	ϕ	[deg]	90	65	20	–	–

[a] We implemented the prior on the electron temperature T_e even if there were values of L_X from the literature to guarantee that the electron temperature satisfies the conditions set out by the approximations in Robinson & Melrose (1984).

Table B1. `emcee` Settings and Results

Star	α	Burn-in	Production	Auto-correlation	Acceptance Frac.
HR 1099	$\frac{3}{2}$	75,000	1,500,000	11,900 (126x)	0.27
UX Arietis	2	2,000	20,000	210 (95x)	0.46
Algol	$\frac{5}{4}$	150,000	2,500,000	31,900 (79x)	0.25
V410 Tau	$\frac{4}{3}$	50,000	1,000,000	7,200 (140x)	0.25
HD 283572	$\frac{5}{4}$	100,000	2,000,000	24,400 (81x)	0.21

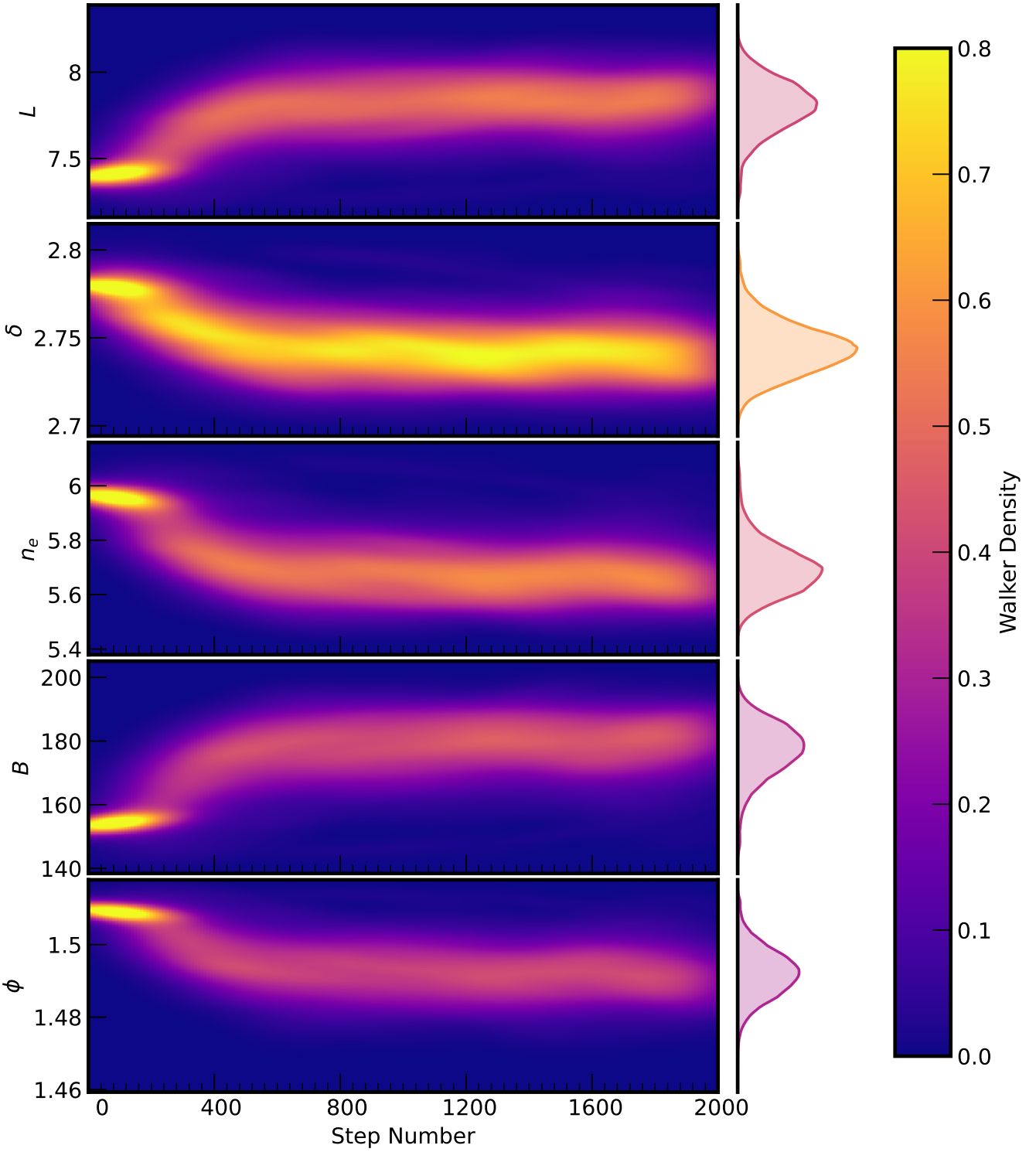

Figure B1. Walker position in each parameter as a function of step number. Convergence of the walkers is obvious by consistent and repeated exploration of the same region of posterior space. The distributions on the right side of each plot indicate the median value of the walker density along that axis. The distribution is shaded according to the maximum of the median values.